The International Conference on Surfaces, Coatings and Interfaces

SurfCoat Korea 2017

29 Mar - 31 Mar 2017 | Incheon - Korea

Conference Proceeding

DOI: https://doi.org/10.26799/cp-sfkorea2017

*Proceedings of the the International Conference on Surfaces, Coatings and Interfaces (**SurfCoat Korea 2017**)*
Incheon - Rep. of Korea – Mar 29 – 31, 2017
DOI: https://doi.org/10.26799/cp-sfkorea2017

Fabrication of Hydrophobic Mesh by NR/SiO_2-encapsulated Fluoroalkylsilane Coating for Oil/Water Separation

J. Saengkaew[1], C. Samart[1], H. Sawada[2], M. Nishida[3] and S. Kongparakul[1*]

[1] Thammasat University, Department of Chemistry,
Faculty of Science and Technology, Pathumthani, Thailand
[2] Hirosaki University, Department of Frontier Materials Chemistry,
Graduate School of Science and Technology, Hirosaki, Japan
[3] National Institute of Advanced Industrial Science and Technology (AIST), Nagoya, Japan

Abstract
The hydrophobic-oleophilic mesh is prepared via simple and environmental friendly method by coating of encapsulation particle. The natural rubber-encapsulated silica (NR/SiO_2) can undergo the chemical reaction with fluoro-containing chemical under alkaline conditions at 6±2 °C to provide the NR/SiO_2-encapsulated fluoroalkylsilane. Firstly, the natural rubber was encapsulated with inorganic silica shell using tetraethyl orthosilicate (TEOS) as a silica precursor. The thermal behavior of surface modified natural rubber from thermogravimetric analysis (TGA) showed the thermal stability enhancement of natural rubber after encapsulated with silica shell. The morphology of NR/SiO_2 from TEM image revealed rubber core covered by silica shell. Secondly, the process is integrated between NR/SiO_2 and fluoroalkylsilane group. The coating mesh exhibited hydrophobic-oleophilic characteristic with static water contact angle (WCA) value of 138° and oil contact angle (OCA) of 0°. The surface roughness of mesh from encapsulation particle coating was confirmed by SEM. The coating surface with these encapsulated particles, NR/SiO_2-encapsulated with trimethoxy(3,3,3-trifluoropropyl)silane (FAS-3) is applicable to use as coating material for oil/water separation

Keywords: natural rubber, encapsulation, fluoroalkylsilane, silica, hydrophobic-oleophilic characteristic, stainless steel mesh, coating, oil/water separation.

1. Introduction

In the past few years, with increasing of industrial oily wastewater and oil spill accidents, oil/water separation has become a worldwide challenge. The methods of treatment oily wastewater have many approaches such as gravity separation, coagulation, oil skimmer, filtration, centrifugal machine, flotation, absorbing materials and combustion [1-5]. On the other hand, most of the methods involve complicated processing steps, long processing time and secondary pollution during the process. The separating materials stand out from a simple, universal and environmentally friendly for oil and water separation [6]. In addition, the surface with hydrophobic/oleophilic wettability has triggered research in the field of filtration [7-8]. The separating materials with special wettability and micro-nanoscale structure have attracted increasing ability of hydrophobic/oleophilic property. The material, which is modified with fluoro-compound features low-surface-energy material due to hydrophobic fluoro-compound ending group. Many types of hydrophobic surface have been created by researcher in resent year. For example, the PU sponges that exhibit superhydrophobicity/superoleophilicity (WCA = 157° and OCA 0°) are fabricated by chemical vapor deposition (CVD) of tetraethoxysilane (TEOS) and then dip-coating in a fluoropolymer (FP) aqueous solution. The sponges show excellent oil stability, and reusability in terms of oil absorbency. The superhydrophobic PU sponges are very promising materials for oil absorption and oil/water separation [9]. The research presents fabricating and evaluating a novel fluorinated polybenzoxazine (F-PBZ) modified nanofibrous membrane optimized to achieve gravity driven oil–water separation. The membrane was prepared by a facile combination of electrospun poly(*m*-phenylene isophthalamide) (PMIA) nanofibers and an *in situ* polymerized F-PBZ functional layer incorporating SiO_2 nanoparticles (SiO_2 NPs) [10]. Hence, fluoro-compound is often to modify with polymer and in order to achieve hydrophobicity [11]. The modified materials are applied to self-cleaning, oil absorption and oil/water separation materials. Natural rubber (NR) is an important polymer from natural resource in Thailand. The NR latex system is outstanding green system more than another polymer [12]. In the present work,

DOI: https://doi.org/10.26799/cp-sfkorea2017

NR particles encapsulated with silica shell which present silanol group on their surface has been synthesized *via* one-pot procedure. Then, the natural rubber-encapsulated silica (NR/SiO_2) was modified with FAS-3 to improve hydrophobic characteristic. The stainless steel mesh, which is dip coated with FAS-3 exhibits hydrophobic and superoleophilic (WCA = 138° and OCA = 0°). The NR/SiO_2 modified FAS-3 mesh diesel oil passes through but blocks water with high separation efficiency even after 30 cycles.

2. Experimental section

2.1. Materials

High ammonia natural rubber latex (60 %dry rubber content) was supplied by Rubber Research Institute, Thailand. Tetraethyl orthosilicate (TEOS) and trimethoxy(3,3,3-trifluoropropyl)silane (FAS-3) were purchased from Sigma-Aldrich while methanol from QRëC. Triton™ X-100 was purchased from ACROS. All chemicals were used without purification.

2.2. Measurements

The particle size measurements were measured by using particle size analyzer (Horiba, Partica LA-950V2 and Nanopartica SZ-100, Japan). Fourier transform infrared (FTIR) spectra were obtained by attenuated total reflection Fourier transform infrared spectrometer (ATR-FTIR, Perkin Elmer, USA) over the wavenumber of 4000 and 650 cm^{-1}.Contact angles of water (WCA) and various oils (OCA) were measured using an optical contact angle meter (TL100, Theta Lite, Finland). The morphology was observed using a transmission electron microscope (TEM, JEM-2100, JEOL, Japan and TECNAI 20 TWIN, Philips, Netherlands) under an electron beam with an accelerating voltage of 120 kV and scanning electron microscope (SEM, JSM-5410 LV, JEOL, Japan). The thermal behaviour of the sample was measured on thermogravimetric analyzer (TGA/SDTA 851^e, Mettler Toledo, Switzerland) under a nitrogen atmosphere with the heating rate of 10°C min^{-1} and operated at 40 to 900°C.

2.3. Preparation of natural rubber-encapsulated silica (NR/SiO_2)

0.5 g of triton X-100 was dissolved in deionized water (DI water) and 15% DRC of natural rubber latex (NR latex) was drop-wised within 25 min through a dropping funnel .Then, 4.8×10^{-3} mol of TEOS was added into this solution and continuously stirred at 6±2 °C for 4 h to form homogeneous milky mixture. The NR/SiO_2 latex was stored at 4 °C .

2.4 Preparation of NR/SiO_2 modified with FAS-3

The mixture containing 6.24×10^{-3} mol of methanol solution, TEOS and FAS 3 with various molar ratio of FAS 3:TEOS were stirred at 6±2 °C . Then, 1 mL of natural rubber-encapsulated silica (NR/SiO_2) was added into this solution and stirred at 6±2 °C for 5 h. The NR/SiO_2-encapsulated fluoroalkylsilane latex was stored at 4 °C .The effect of various FAS 3:TEOS mole ratio (1:1, 1.6:1, 2:1 and 2.6:1) was studied.

2.5 Surface modification of mesh and oil/water separation experiment

The stainless steel meshe (#150) was cleaned in an ultrasonic bath with acetone for 30 min and DI water for 30 min to remove surface impurities. The meshes were dipped in NR/SiO_2 modified with FAS-3 latex at room temperature, left for 3 min and these were dried at 80 °C.

The oil/water separation experiment: The device consists of two tubes, which are 100 mm and 100 mm in length, respectively, and 25 mm in diameter. The hydrophobic nature of the coatings was tested with oil/water separation experiment. The mesh was fixed between two tubes by four screw. The hexane (dyed with Oil Red O)/water (dyed with copper sulfate) mixture (50% v/v) was poured onto the mesh and then the separation was proceeded by gravity.

3. Results and discussion

The natural rubber-encapsulated silica **(**NR/SiO_2**)** was prepared with sol-gel reaction under alkaline condition**.** The encapsulated material based on natural rubber core and inorganic silica shell was modified with fluoroalkylsilane compound **(**FAS-3**)** for dip-coating on stainless steel mesh to separate oil/water mixture (Figure 1). The fluoroalkylsilane should be modified through the chemical reaction between the hydroxyl group in FAS-3 and silanol group on surface of NR/SiO_2 under alkaline condition**.** The structure of functional shell was analysed using

DOI: https://doi.org/10.26799/cp-sfkorea2017

FTIR (Table 1) and ^{29}Si solid-state NMR spectroscopy. The spectrum of NR/SiO_2 shows the peak at 3289 and 1097 cm^{-1} that are attributed to silanol group (Si-OH) and Si-O-Si bonding, respectively. The peaks appear at 2961-2851, 1436 and 1376 cm^{-1} referred to NR group. In the NMR spectrum of NR/SiO_2, the peak at -125.1 and -93.4 ppm are attributed to *Si*(Si-O) (call Q^4, siloxane bridges) and (Si-O)$_3$*Si*-OH (Q^3), respectively. Therefore, it can confirm the successful encapsulation of NR within the silica shell.

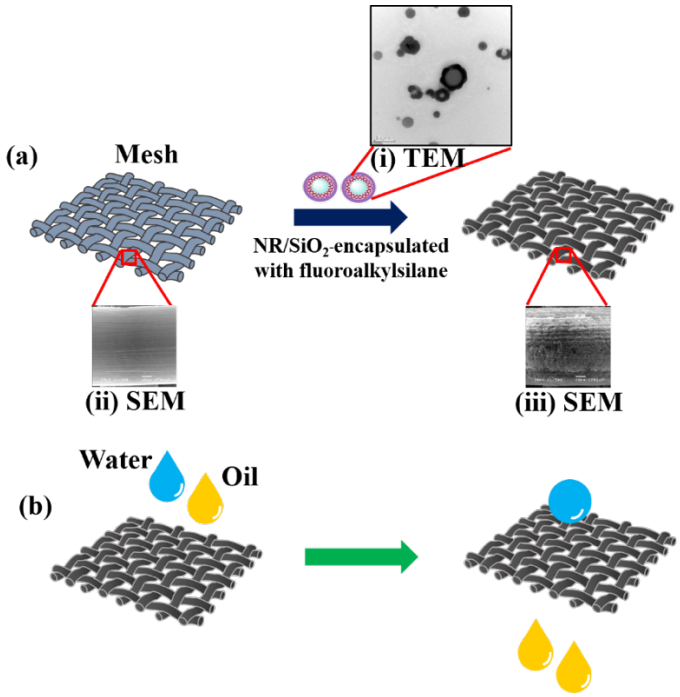

Figure 1: Figure illustrating the stainless steel mesh for oil/water separation: (a) when dipped into NR/SiO_2 modified with fluoroalkylsilane latex system for 3 min, the mesh exhibits hydrophobic-superoleophilic characteristic; the inset TEM image of (i) NR/SiO_2 particles (scale bar, 0.5 µm) and SEM images of (ii) before and (iii) after coating. (b) After mesh was coated with NR/SiO_2 modified fluoroalkylsilane, oil can penetrate though the mesh but water cannot.

Table 1: The FTIR characteristic of NR/SiO_2

Wavenumber (cm^{-1})	Peak designation
1097	Si-O-Si stretching
1376	-CH- deformation
1436	-CH_2- deformation
2961	-CH_2- symmetric stretching
2920	-CH_2- asymmetric stretching
2851	-CH_3 stretching
3289	Si-OH stretching

Encapsulation of NR with silica improved the thermal properties that was investigated by thermogravimetric analyses (TGA). The maximum temperature of decomposition (T_{max}) values of NR and NR/SiO_2 are 391 and 403.9 °C. From the data, T_{max} value of NR/SiO_2 is higher than NR that it is attributed to the effect of silica shell. The morphology of encapsulation was observed by TEM images (Figure 1(i)). The electronic density of silica is much larger than natural rubber latex particle. Therefore, the silica appears as black or dark grey particles, which fully encapsulated NR particles. The average diameter of NR/SiO_2 is 0.8±0.2 µm.

DOI: https://doi.org/10.26799/cp-sfkorea2017

The surface morphology of mesh was observed by SEM images. The Figure 1 shows SEM image of uncoated and NR/SiO_2 modified FAS-3 stainless steel mesh. The uncoated mesh shows a smooth surface however NR/SiO_2 modified FAS-3 mesh displays a surface roughness at FAS-3:TEOS mole ratio of 2:1. The effect of various mole ratio of FAS- 3:TEOS (1:1, 1.6:1, 2:1 and 2.6:1) was studied in part of preparation NR/SiO_2 modified with FAS-3. Table 2 shows stability and water contact angle (WCA) of NR/SiO_2 modified FAS-3 with different FAS-3:TEOS mole ratio. The WCA of NR/SiO_2 modified FAS-3 mesh with 1:1, 1.6:1 and 2:1 mole ratio are 106.9, 121 and 138°, respectively. An oil droplet with a low surface tension quickly spreads on surface of NR/SiO_2 modified FAS-3 mesh and permeates through it, exhibiting a highly oleophilic property (OCA of 0°). The water contact angle increases from increasing of fluoroalkylsilane concentration while the WCA and OCA of uncoated mesh are 77.5 and 15.6°, respectively. It seems that hydrophobicity mainly comes from the FAS concentration.

In the meanwhile, at FAS-3:TEOS mole ratio above 2:1 the latex suspension suddenly coagulates because of the different polarity between the NR/SiO_2, TEOS and fluoroalkylsilane. As a result, The FAS-3:TEOS mole ratio of 2:1 is suitable condition for this system. A trend was observed where the WCA of NR/SiO_2 modified FAS-3 mesh increased with fluoroalkylsilane concentration. Consequently, fluoroalkylsilane is the key factor to form the modification particles as well as the hydrophobic and superoleophilic mesh.

A combination of hydrophobic and superoleophilic, the NR/SiO_2 modified FAS-3 mesh has great potential to be applied to an oil/water separation. As shown in Figure 2(c), the NR/SiO_2 modified FAS-3 mesh was placed between two glass tubes. Then a mixture of hexane and water (50% v/v of oil) was poured into the upper tube. The oil quickly permeated through the hydrophobic/superoleophilic NR/SiO_2 modified FAS-3 mesh and dropped into the beaker below, whereas the water layer remained above the mesh. The oil/water separation procedure was realized by gravity and no external force. The collected oil was very clear with no visible water in the oil, indicating a high oil/water separation efficiency. In the meanwhile, the oil/water mixture pass through the uncoated mesh (Figure 2(b)).

Additionally, the oil/ water separation system could be reused continuously. In this experiment, the NR/ SiO_2 modified FAS-3 mesh works well even after recycling 30 times; no visible water residuals and separation efficiency of >92%. Oil/water separation efficiency is used to quantitatively describe the oil/water separation ability of the as-prepared stainless steel mesh. Because the hydrophobic layer is robust so the as-prepared mesh can be reused. The recycling ability was investigated by taking the oil/water mixture as an example.

The separation efficiency (η, expressed as a percentage) was determined with the following equation (1):

$$\eta = \left(\frac{m_1}{m_0}\right) \times 100\% \quad (1)$$

where; m_0 and m_1 are the mass of the rejected aqueous phase before and after the separation process, respectively [13].

Table 2: The stability and water contact angle (WCA) of NR/SiO_2 modified FAS-3 mesh with different FAS-3:TEOS mole ratio

run	FAS-3:TEOS mole ratio	WCA (°)	Stability of latex
1	1:1	106.9	Milky fluid
2	1.6:1	121	Milky fluid
3	2:1	138	Milky fluid
4	2.6:1	N/A	Coagulation

DOI: https://doi.org/10.26799/cp-sfkorea2017

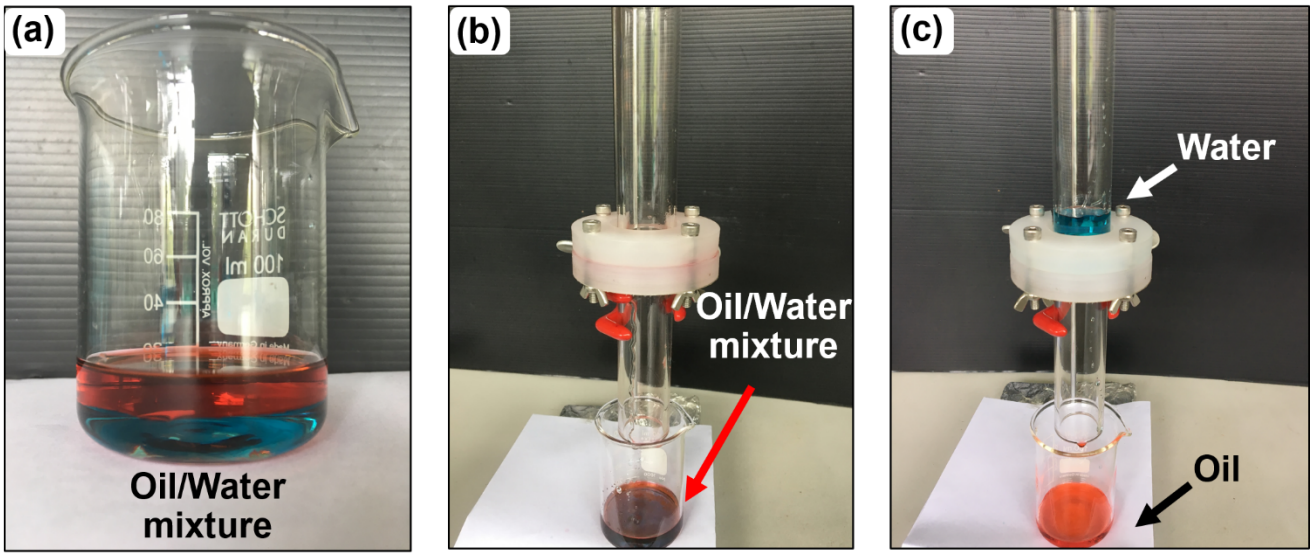

Figure 2: (a) The mixture of hexane and blue-colored aqueous solution (hexane was dyed by Oil Red O and water was dyed by copper (II) sulfate). Separation of oil/water by using (b) uncoated mesh and (c) NR/SiO_2 modified FAS-3 mesh under atmospheric conditions.

4. Conclusion

In conclusion, the hydrophobic and superoleophilic oil/water separation mesh was successfully prepared by dip-coating a stainless steel mesh with the NR/SiO_2 modified FAS-3 latex. The NR/SiO_2 modified FAS-3 mesh surface not only exhibits hydrophobicity, with a water contact angle (WCA) of 138°, but also superoleophilicity with an oil contact angle (OCA) of 0°. In addition, the oil/water mixtures was observed to be separated by the mesh with a separation efficiency of >92% that it remained high even after 30 cycles. The fabrication process is facile environmentally friendly and great in application. Because of the excellent oil/water performance, the NR/SiO_2 modified FAS-3 mesh has potential application in industrial oil/water mixtures and environmental oil spills.

Acknowledgements

The authors gratefully acknowledge the financial support from the Thailand Research Fund (DPG 6080001). This research is supported by Department of Chemistry, Faculty of Science and Technology, Thammasat University and Central Scientific Instrument Center, Thammasat University. The authors are grateful to Prof. Hideo Sawada and Dr. Masakazu Nishida from Japan for their comments and support of the NMR measurement.

References

1. I. Zouboulis and A. Avranas, “Treatment of oil-in-water emulsions by coagulation and dissolved-air flotation,” *Colloids Surf., A,* vol. 172, pp. 153-161, 2016.
2. H. Zhu, D. Chen , N. Li, O. Xu, H. Li, J. He and J. Lu, “Dual-layer copper mesh for integrated oil-water separation and water purification, ” *Appl .Catal., B,* vol. 200, pp. 594-600, 2000.
3. P. Calcagnile, D. Fragouli, I. S. Bayer, G. C. Anyfantis, L. Martiradonna, P. D. Cozzoli, R. Cingolani and A. Athanassiou, “Magnetically Driven Floating Foams for the Removal of Oil Contaminants from Water, ” *ACS Nano*, vol. 6, no. 6, pp. 5413-5419, 2012.
4. T. Yuan, J. Meng, T. Hao, Z. Wang and Y. Zhang, “A Scalable Method toward Superhydrophilic and Underwater Superoleophobic PVDF Membranes for Effective Oil/Water Emulsion Separation,” *ACS Appl. Mater. Interfaces*, vol. 7, no. 27, pp. 14896–14904, 2015.

DOI: https://doi.org/10.26799/cp-sfkorea2017

5. Q. Liu, A. A. Patel, and L. Liu," Superhydrophilic and Underwater Superoleophobic Poly(sulfobetaine methacrylate)-Grafted Glass Fiber Filters for Oil–Water Separation," *ACS Appl. Mater. Interfaces*, vol. 6, no. 12, pp. 8996–9003, 2014.
6. Y. Liu, K. Zhang, W. Yao, C. Zhang, Z. Han and L. Ren, "A Facile Electrodeposition Process for the Fabrication of Superhydrophobic and Superoleophilic Copper Mesh for Efficient Oil–Water Separation," *Ind. Eng. Chem. Res*., vol. 55, no. 10, pp. 2704–2712, 2016.
7. Z. Yu, J. Ni, L. Fang, D. Wu and H. Zhu, "Multilayer Three-Dimensional Structure Made of Modified Stainless Steel Mesh for in Situ Continuous Separation of Spilled Oil," *Ind. Eng. Chem. Res*., vol. 54, no. 47, pp. 11838-11843, 2015.
8. G. J. Dunderdale, C. Urata, T. Sato, M. W. England and A. Hozumi, "Continuous, High-Speed, and Efficient Oil/Water Separation using Meshes with Antagonistic Wetting Properties," *ACS Appl. Mater. Interfaces*, vol. 7, no. 34, pp. 18915–18919, 2015.
9. L. Wu, L. Li, B. Li, J. Zhang and A. Wang, "Magnetic, Durable, and Superhydrophobic Polyurethane@Fe_3O_4 @SiO_2@Fluoropolymer Sponges for Selective Oil Absorption and Oil/Water Separation," *ACS Appl. Mater. Interfaces*, vol. 7, no. 8, pp. 4936–4946, 2015.
10. X. Tang, Y. Si, J. Ge, B. Ding, L. Liu, G. Zheng, W. Luo and J. Yu, "In situ polymerized superhydrophobic and superoleophilic nanofibrous membranes for gravity driven oil–water separation," *Nanoscale*, vol. 5, pp. 11657-11664, 2015.
11. Y. Oikawa, T. Saito, S. Yamada, M. Sugiya and H. Sawada, "Preparation and Surface Property of Fluoroalkyl End-Capped Vinyltrimethoxysilane Oligomer/Talc Composite-Encapsulated Organic Compounds :Application for the Separation of Oil and Water," *ACS Appl. Mater. Interfaces*, vol. 7, no. 25, pp. 13782-13793, 2015.
12. S. Poompradub, M. Thirakulrati and P. Prasassarakich, "In situ generated silica in natural rubber latex via the sole gel technique and properties of the silica rubber composites," *Mater. Chem. Phys*., vol. 144, pp. 122-131, 2014.
13. J. Li, D. Li, Y. Yang, J. Li, F. Zha and Z. Lei, "A prewetting induced underwater superoleophobic or underoil (super) hydrophobic waste potato residue-coated mesh for selective efficient oil/water separation," *Green Chem*., vol. 18, pp. 541-549, 2016.

*Proceedings of the the International Conference on Surfaces, Coatings and Interfaces (**SurfCoat Korea 2017**)*
Incheon - Rep. of Korea – Mar 29 – 31, 2017
DOI: https://doi.org/10.26799/cp-sfkorea2017

Enhanced shielding effectiveness for electromagnetic wave radiation using carbon nanocoil-carbon microcoil hybrid materials

Gi-Hwan Kang, Sung-Hoon Kim*, and Sangmoon Park

Department of Engineering in Energy & Applied Chemistry, Silla University, Busan 617-736, Republic of Korea
*Corresponding author: Fax: +82-(51)-999-5335, E-mail address: shkim@silla.ac.kr

Abstract:
The formation of carbon nanocoil-carbon microcoil (CNC-CMC) hybrid materials, namely, the formation of numerous carbon nanocoils (CNCs) on the surface of carbon microcoils (CMCs), was achieved by using C_2H_2 as the source gas and CS_2 as the additive gas in a thermal chemical vapor deposition system. During the reaction, CS_2 was injected into the reactor in modulated on/off cycles. The density of CNCs formed on the surface of CMCs increased with increasing on/off cycle numbers. In the as-grown state, the CNC-CMC hybrid materials showed higher electrical conductivity values than those of materials composed of CMCs only. Composites of CNC-CMC hybrid materials in polyurethane (CNC-CMC@PU) and CMCs in polyurethane (CMC@PU) were fabricated. The CNC-CMC@PU composites showed higher shielding effectiveness than CMC@PU composites, irrespective of the mixing ratios of carbon nanomaterials in PU. Based on the obtained shielding effectiveness and electrical conductivity values, we conclude that the formation of CNC-CMC hybrid materials can enhance shielding effectiveness through a reflection-based mechanism as well as an absorption-based mechanism.

Keywords: Carbon nanocoil-carbon microcoil hybrid materials, CS_2 gas flow, Cycling modulation, Thermal chemical vapor deposition, Electromagnetic wave shielding effectiveness

1. Introduction

Owing to their unique helix-type geometries, carbon-coil-based hybrid materials, which are composed of carbon microcoils (CMCs) and various types of carbon nanomaterials, such as carbon nanofibers (CNFs) and carbon nanocoils (CNCs), have received increasing attention [1–3]. The DNA-like double-helix-type coil geometries of CMCs are regarded as promising electromagnetic wave absorbers because they appear to induce an electrical current through an inductive electromotive force, thus generating a magnetic field [4, 5]. Furthermore, compared with metals, carbon composites are lightweight and moldable. Therefore, carbon-based hybrid materials and composites are regarded as promising materials to replace metals that are commonly used as electromagnetic wave shielding materials [6–10].

In general, reflection and absorption of electromagnetic wave radiation are regarded as the main shielding mechanisms for electromagnetic interference [11–13]. Materials that operate via the reflection mechanism should have high electrical conducting properties [11], whereas materials that operate via the absorption mechanism require sufficient electric constants or magnetic permeability [12]. The reflection property decreases with increasing operating frequency, whereas the absorption property increases with increasing operating frequency [13]. In addition, only the absorption property is proportional to the thickness of the shield [13].

DOI: https://doi.org/10.26799/cp-sfkorea2017

Nowadays, the operating frequencies of mobile electronic devices require the use of a higher frequency region to correspond to the huge amounts of data transfer in current mobile devices. Therefore, shielding materials for electromagnetic waves should have enhanced electromagnetic wave absorption characteristics to operate in the higher frequency region. In this respect, helix-type CMC-based hybrid materials are more attractive because the helix-type coil geometries in CMC-based hybrid materials have an effective form for absorbing electromagnetic waves by inducing an electric current [4, 5]. Furthermore, the hybrid connections in CMC-based hybrid materials may give rise to electron-conducting channels. Consequently, the shielding characteristics might be enhanced, even in the low operating frequency region, owing to the higher electrical conductivity. In these respects, CMC-based hybrid materials are strongly appealing as promising materials for application as shielding materials for electromagnetic waves, either in the low or high operating frequency regions.

Because the metal catalyst used for the formation of carbon nanomaterials could easily diffuse into the carbon substrate during reaction, the formation of carbon nanomaterial-based hybrid materials has been very difficult [14, 15]. Up to now, only a few attempts, such as the injection-gas-flow on/off modulation method and the two-step method, have been made to address this drawback in the formation of CMC-based hybrid materials [3, 16, 17]. In the injection-gas-flow on/off modulation method, the growth of CNCs occurred directly on the surface of the CMCs [3]. For the two-step method, Ni nanoparticles were first coated on the prepared carbon fibers by a precipitation-reduction technique, and then CMCs were deposited on the surface of the Ni-nanoparticle-coated carbon fibers [16, 17]. In the two-step method, the relatively large-sized carbon fibers were prepared first, and then the CMCs grown on the prepared carbon fibers. On the other hand, in the on/off modulation method, CMC-based hybrid materials, namely, numerous CNCs on CMCs, could be simultaneously obtained. Consequently, the on/off modulation method may give rise to an increased formation density of hybrid materials, as well as improved usability of the process.

Previously, we introduced an on/off cycling method with SF_6 to form carbon coil-based hybrid materials [3]. In this work, we present the formation of CNC-CMC hybrid materials using stepwise on/off cycles of CS_2 gas flow. The morphologies of the CNC-CMC hybrid materials were investigated as a function of the stepwise on/off cycle number. In the as-grown state, the electrical conductivity values of the CNC-CMC hybrid materials were measured and compared with those of carbon nanomaterials composed of CMCs only. The electromagnetic wave shielding properties of CNC-CMC hybrid materials in polyurethane (CNC-CMC@PU) composites were examined according to the mixing ratio of the CNC-CMC hybrid materials in PU and the composite layer thickness across the operating frequency range of 1.25–4.0 GHz. Based on these results, we discuss the characteristics of the shielding effectiveness of CNC-CMC@PU composites compared with those of CMCs in polyurethane (CMC@PU) composites.

2. Experimental

As a catalyst to form the carbon nanomaterials, approximately 0.01 g of Ni powder (99.7 %) with particle diameters ranging from 10 to 100 μm was spread onto an alumina substrate. A thermal chemical vapor deposition (TCVD) system was employed for the deposition of carbon coils, using C_2H_2 as the source gas and CS_2 as the additive gas. The flow rate of C_2H_2 was set at 500 standard cm^3 per minute (sccm), and the flow rate of CS_2 was adjusted from 20 to 100 sccm. The substrate temperature and the total pressure in the reactor during the reaction were set at 750 °C and 100 Torr, respectively. The detailed reaction conditions for the formation of the CNC-CMC hybrid materials are shown in Table 1.

DOI: https://doi.org/10.26799/cp-sfkorea2017

In this work, cyclic modulation of the CS_2 gas flow was carried out simply by modulating the gas flow and switching the gas flow on and off in continuous cycles. The source gas flow sequence mirrored the iterative order of the reaction processes: $C_2H_2 + CS_2$ flow (C_2H_2 flow on and CS_2 flow on) followed by C_2H_2 flow (C_2H_2 flow on and CS_2 flow off). The cycling period was defined as the time the source gas was composed of both C_2H_2 and CS_2, plus the time the source gas consisted of C_2H_2 only. For one cycle, the CS_2 flow injection on and off times were set at 12.5 and 12.5 min, respectively, resulting in a total duration of 25 min for one cycle. During the CS_2 flow injection on time, the flow rate of CS_2 was varied in a stepwise manner. First, the flow rate of CS_2 was set at 100 sccm for 4.0 min and then reduced to 20 sccm for 8.5 min. Three processes, each with a different cycling modulation number, were carried out. The cycling numbers for these processes were 1, 2, and 4, respectively. The total injection times of CS_2 during the processes were thus maintained at 12.5, 25.0, and 50.0 min, respectively. For comparison, a process with continuous CS_2 flow, namely, continuous $C_2H_2 + CS_2$ flows, was also carried out. Figure 1 shows the details of each process.

The morphologies and chemical compositions of the samples were investigated in detail using field-emission scanning electron microscopy (FESEM; S-4200, Hitachi) coupled with energy dispersive X-ray spectroscopy (EDS). The nanostructures of the CMCs and CNCs were examined by high-resolution transmission electron microscopy (HRTEM; JEM 2011, JEOL). The samples for HRTEM were prepared by dispersing the materials in acetone using an ultrasonic bath. Droplets of the obtained suspension were placed onto a carbon film supported by a Cu grid. The Cu grid was then placed into the HRTEM chamber, and images of the detailed morphologies of the samples were obtained. The resistivity (Ω cm) of the samples in the as-grown state was measured with a four-point probe (labsysstc-400, Nextron) using Ohm's law and a correction factor at room temperature [18].

For the CNC-CMC@PU composites, the CNC-CMC hybrid materials were dispersed in PU with the addition of dimethylformamide (DMF) using an ultrasonic system. The molecular weight of PU used in this work was in the range of 60,000–70,000. After 120 min of on/off ultrasonic treatment at 500 W and 20 kHz, a paste-type CNC-CMC hybrid material-PU-DMF mixture was obtained. For comparison, a CMC-PU-DMF mixture was also prepared using the same procedure. Indeed, four paste-type CNC-CMC hybrid material-PU-DMF mixtures (CNC-CMC@PU) or paste type CMC-PU-DMF mixtures (CMC@PU) were prepared, as summarized in Table 2. After fabricating the four paste-type samples, each sample was coated onto a circular-shaped glass plate with a diameter of 133 mm by pouring about 20 mL of the paste-type sample onto the glass plate and then drying the samples naturally in a fume hood for about 24 h. Finally, the weights of the coated samples were measured using an electronic balance (BJ210s, Sartorius).

The shielding effectiveness (SE) of the CNC-CMC@PU composites was analyzed using a network analyzer (SynthNV2_3b, Windfreak Technologies) in accordance with ASTM D4935-99. The setup consisted of a sample holder with its exterior connected to the network analyzer (see Fig. 2a). A coaxial sample holder (Electro Matrix EM-2107A) and coaxial transmission test specimen were setup according to ASTM D4935-99, as shown in Fig. 2b. The SE measurements for the CNC-CMC@PU composites were performed in the range of 1.25–4.0 GHz.

3. Results and Discussion

The formation of CNC-CMC hybrid materials were first examined by increasing the flow rate of CS_2 from 20 to 100 sccm, namely, steady-state CS_2 flows of 20, 60, and 100 sccm. Figure 3 shows FESEM images of the surface morphologies of samples I, II, and III, which were prepared under the same experimental conditions except the CS_2 flow rate. A comparison of Fig. 3a with Figs. 3b and

DOI: https://doi.org/10.26799/cp-sfkorea2017

3c indicates that the formation of tiny bush-like carbon nanomaterials is achieved under higher flow rates of CS_2. Magnification of the image in Fig. 3b shows the formation of wave-like CNCs around the CMCs (dotted circle, Fig. 3b-i). Therefore, in this work, we named these kinds of carbon structures as CNC-CMC hybrid materials. The bush-like carbon nanomaterials were identified as wave-like CNCs (Fig. 3b-ii). Indeed, sparse formation of the CNC-CMC hybrid materials was observed under higher CS_2 flow rate conditions, namely, a CS_2 flow of 20 sccm (Figs. 3b and 3c). The results shown in Fig. 3 indicate that the formation of CNC-CMC hybrid materials is strongly related to the magnitude of the CS_2 injection flow.

As shown in Fig. 3, the formation of the CMCs is favored at lower CS_2 flow rates, namely, at 20 sccm, whereas the formation of the tiny wave-like CNCs is promoted under higher CS_2 flow rate conditions, namely, above 20 sccm. Therefore, we introduced a stepwise injection flow scheme for CS_2 (process V, Fig. 1), namely, CS_2 is first injected at a higher flow rate (100 sccm) followed by injection at a lower flow rate (20 sccm) to enhance the formation of CNC-CMC hybrid materials on the substrate. Figure 4 shows FESEM images and high-magnification FESEM images of the surface morphologies of samples IV and V. For sample IV, which was prepared under a continuous $C_2H_2 + CS_2$ flow (process IV) for 25 min, only the formation of CMCs was observed (Fig. 4a). However, for sample V, which was prepared by subjecting the substrate to a stepwise on/off injection flow of CS_2, namely, 1 cycle of 12.5 min/12.5 min on/off CS_2 flow (process V), narrow line-shaped structures with sporadic bush-like shapes were observed on the substrate surface (Fig. 4b). The narrow line-shaped structures were proved to be typical double-helix-type CMCs, as shown in the inset of Fig. 4b. The sporadic bush-like shapes were confirmed as wave-like CNCs (inset, Fig. 4b), which seemed to be gathered around the CMCs. Consequently, it was confirmed that the formation of CNC-CMC hybrid materials, namely, the formation of wave-like CNCs around CMCs, can be achieved by stepwise cyclic modulation of the CS_2 flow.

Figure 5 shows FESEM images and high-magnification FESEM images of the surface morphologies of samples VI and VII. As the number of CS_2 flow cycles increased from 1 (sample V) to 2 (sample VI), line-shaped structures, similar to those on the sample V, were also observed on the substrate in sample VI (Fig. 5a). These structures were proved to be partly composed of wave-like CNCs formed on the surfaces of CMCs, as shown in the inset of Fig. 5a. For sample VII, which was prepared with the highest number of CS_2 flow cycles in this work (process VII), most of the surfaces of the CMCs seem to be covered by wave-like CNCs, as shown in Fig. 5b, which look like the frosted branches of shrubs (Fig. 5b-i). The CMCs, located in the middle of the frosted-branch structures, seem to serve as a backbone to support the numerous CNCs. The CNCs might be attached to the surfaces of the supporting CMCs (Fig. 5b-ii). These combined results, as shown in Figs. 3–5, strongly indicate that the formation of wave-like CNCs around CMCs is strongly related to the higher injection flow of CS_2. Therefore, increasing the proportion of higher CS_2 injection flow by increasing the number of CS_2 injection flow cycles could increase the number of tiny wave-like CNCs on the surfaces of CMCs in CNC-CMC hybrid materials. In addition, tiny wave-like CNCs seemed to be produced under a flow of excess C_2H_2, as previously reported [3]. Therefore, a higher number of CS_2 flow cycles might increase the number of tiny wave-like CNCs.

Detailed images of the carbon filaments constituting the CNC-CMC hybrid materials (sample VI) were analyzed by TEM, as shown in Fig. 6. Several protruding points (dotted circles, inset, Fig. 6) were observed in the wave-like CNCs. As shown in Fig. 7, the presence of Ni at the protruding points of the CNCs was confirmed by examination of the wave-like CNCs using FESEM and EDS. According to the dissolution-diffusion-precipitation model [19] of carbon nanofilaments, the metal catalyst, usually Ni, detected at protruding points corresponds to the starting points for the

DOI: https://doi.org/10.26799/cp-sfkorea2017

formation of carbon nanofilaments. Therefore, the protruding points observed in the wave-like CNCs in Fig. 6 would be the starting points, namely, the heads, for the formation of the wave-like CNCs. As shown in the inset of Fig. 6, the heads of the wave-like CNCs existed on the exterior of the CMCs. Examination of the wave-like CNCs indicated by the dotted square in Fig. 6 shows that the wave-like CNCs are attached onto the surface of the CMC. Therefore, the wave-like CNCs in the CNC-CMC hybrid materials are considered to grow from the surfaces of the CMCs, as previously reported [3]. Figure 8 shows FESEM images of CMCs with CNCs in different states of development in sample V. The growth of CNCs seems to be initiated on the surfaces of the CMC (Fig. 8b) and they are developed (Fig. 8c). Finally, the CNCs grow from the surfaces of the CMC, as shown in Fig. 8d. These images also confirm the development of the CNCs directly from the surface of the amorphous-carbon (a-carbon) structure constituting the CMC, as previously reported [3].

The resistivity values of as-gown samples I and VII were measured three times under vacuum conditions. Figure 9 shows the resistivity values of sample I (CMCs only) and sample VII (CNC-CMC hybrid) on increasing the operating temperature from 20 to 300 °C. Both samples show decreased resistivity with increasing operating temperature, indicating semiconductor characteristics. Moreover, the resistivity values of sample VII are lower than those of sample I across the entire range of operating temperatures. This result indicates that the formation of CNC-CMC hybrid samples can enhance electrical conductivity, regardless of the operating temperature. Furthermore, the standard deviations of the resistivity values for the CNC-CMC hybrid sample were considerably reduced compared with those of the CMC-only sample. Therefore, it is believed that the formation of CNC-CMC hybrid materials can enhance and stabilize electrical conductivity. Based on these results, electron-conducting channels might be formed by the formation of CNCs on the surfaces of CMCs via the connection of CNCs to CMCs, as previous reported [20]. Such electron-channels may play a role in enhancing and stabilizing the electrical conductivity values.

The effectiveness of the CNC-CMC@PU composites for shielding electromagnetic waves was examined using sample VII, which was made using the highest number of on/off cycle numbers in this work. The CNC-CMC@PU composites were compared with that of CMC@PU composites in the operating frequency range of 1.25–4.0 GHz. We prepared two kinds of paste-type samples (samples A and B) with different mixing ratios of CNC-CMC hybrid materials, PU, and DMF, as shown in Table 2, for comparison with CMC@PU composites prepared under the same mixing ratio conditions (samples C and D). The total thickness of the coating layers in samples A–D was measured as a function of the number of coatings, showing a gradual increase as more layers were deposited (Fig. 10). Compared with the other samples, the thickness of the coating layers was slightly higher for samples A and B, namely, the CNC-CMC@PU composites. This difference appears to be due to the slightly higher volume-to-weight ratios of the CNC-CMC hybrid materials compared with those of the CMCs.

To evaluate the shielding efficiency of the composites, we first investigated the variation in the SE values for samples A–D with similar layer thicknesses (~3 mm) at increasing operating frequencies, as shown in Fig. 11. For the composites, the SE values exhibited an overall tendency to increase with increasing operating frequency (Fig. 11). As indicated by Simon's empirical equation, absorption-based SE increases with increasing operating frequency [21]. Therefore, these samples apparently show behavior that is typical of an absorption-based shielding mechanism.

Variations in the SE values of the CNC-CMC@PU composite (sample A) and the CMC@PU composite (sample C) with operating frequency were also investigated for different composite

DOI: https://doi.org/10.26799/cp-sfkorea2017

thicknesses. The SE values of samples A and C with thicknesses of 0.8–3.1 mm increased over the operating frequency range of 1.25–4.0 GHz with the increase in the coated-layer thickness (Fig. 12). As indicated by Simon's empirical equation, absorption-based SE is strongly dependent on the composite thickness [21]. Thus, we could confirm that absorption served as a major electromagnetic interference (EMI)-shielding mechanism in the CNC-CMC@PU and CMC@PU composites.

Meanwhile, the SE values of samples C and D (CMC@PU composites) were lower than those of samples A and B, respectively, as shown in Fig. 11. It was considered that these lower SE values of samples C and D were partly due to the lower electrical conductivities of the as-grown CMCs compared with the as-grown CNC-CMC hybrid materials (Fig. 9). Therefore, a reflection-based shielding mechanism originating from the higher electrical conductivities of samples A and B can also be regarded as a primary factor for enhanced SE values of the CNC-CMC@PU composites.

Previously, we reported the SE characteristics of CNC+CMC@PU composites that had been fabricated by mixing CNCs, CMCs, and PU [20]. Compared with those of the CMC@PU composites, the SE values of the CNC+CMC@PU composites were diminished, although they showed slightly higher electrical conductivity values than the CMC@PU composite. The deterioration of the electromagnetic-wave-absorption capability of CMCs by the incorporation of CNCs was suggested as the cause of the decreased SE values for the CNC+CMC@PU composites. In this work, however, the SE properties of CNC-CMC@PU composites, which were fabricated using CNC-CMC hybrid materials and PU, were enhanced compared with those of CMC@PU composites. Therefore, it is suggested that the CNC-CMC@PU composites, unlike the CNC+CMC@PU composites, enhance or at least maintain the electromagnetic-wave-absorption capability of CNCs. Furthermore, the higher electrical conductivity values of the as-grown CNC-CMC hybrid materials compared with those of the as-grown CMCs are believed to contribute to the increase in the SE values of the CNC-CMC@PU composites.

4. Conclusions

The formation of CNC-CMC hybrid materials was successfully achieved by simple modulation of stepwise CS_2 injection flow using on/off cycles. The increase in the amount of CS_2 injected achieved by increasing the number of stepwise CS_2 injection flow cycles increased the number of tiny wave-like CNCs on the surfaces of the CMCs in the CNC-CMC hybrid materials. The formation of CNCs around CMCs may have enhanced and stabilized the electrical conductivities of the samples owing to electron-conducting channels arising from connection of CNCs with CMCs. CNC-CMC@PU or CMC@PU composites were fabricated using CNC-CMC hybrid materials or CMCs with DMF in PU. The SE values of the CNC-CMC@PU composites were higher than those of the CMC@PU composites, irrespective of the mixing ratios of carbon nanomaterials in PU. The electromagnetic-wave-absorption capability was enhanced or at least maintained in the CNC-CMC@PU composites compared with that in the CMC@PU composites. Furthermore, the enhanced electrical conductivity values of the as-grown CNC-CMC hybrid materials are believed to increase the SE values of the CNC-CMC@PU composites.

Acknowledgements

This research was financially supported by the Human Resource Training Program for Regional Innovation and Creativity (2014 H1C1A1066859) and by the Basic Science Research Program (2013R1A1A2007157) through the Ministry of Education and National Research Foundation of Korea.

DOI: https://doi.org/10.26799/cp-sfkorea2017

References

1. Liu L, Zhou K, He P, Chen T, Synthesis and microwave absorption properties of carbon coil-carbon fiber hybrid materials, Mater. Lett. 110 (2013) 76–79.
2. Liu L, He P, Zhou K, Chen T. Microwave absorption properties of carbon fibers with carbon coils of different morphologies (double microcoils and single nanocoils) grown on them, J. Mater. Sci. 49 (2014) 4379–4386.
3. G.-H. Kang, S.-H. Kim, S. Park, Controllablle synthesis of carbon nanocoil-carbon microcoils hybrid materials, Mater. Design, 116 (2017) 42–50.
4. Motojima S, Hoshiya S, Hishikawa Y, Electromagnetic wave absorption properties of carbon microcoils/PMMA composite beads in W bands, Carbon 41 (2003) 2658–2660.
5. Zhao D, Shen Z, Preparation and microwave absorption properties of carbon nanocoils, Mater. Lett. 62 (2008) 3704–3706.
6. Song WL, Wang J, Fan LZ, Li Y, Wang CY, Cao MS, Interfacial engineering of carbon nanofiber-graphene-carbon nanofiber heterojunctions in flexible lightweight electromagnetic shielding networks, ACS Appl. Mater. Interface 6 (2014) 10516–10523.
7. Song WL, Fan LZ, Cao MS, Lu MM, Wang CY, Facile fabrication of ultrathin graphene papers for effective electromagnetic shielding, J. Mater. Chem. C 2 (2014) 5057–5064.
8. Chen Z, Xu C, Ma C, Ren W, Cheng HM, Lightweight and flexible graphene foam composites for high-performance electromagnetic interference shielding, Adv. Mater. 25 (2013) 1296–1300.
9. Cao MS, Wang XX, Cao WQ, Yuan J, Ultrathin graphene: electrical properties and highly efficient electromagnetic interference shielding, J. Mater. Chem. C 3 (2015) 6589–6599.
10. Paliotta L, Bellis GD, Tamburrano A, Marra F, Rinaldi A, Highly conductive multilayer-graphene paper as a flexible lightweight electromagnetic shield, Carbon 89 (2015) 260–271.
11. Wu J, Chung DDL, Increasing the electromagnetic interference shielding effectiveness of carbon fiber polymer-matrix composite by using activated carbon fibers, Carbon 40 (2002) 445–447.
12. Chung DDL, Electromagnetic interference shielding effectiveness of carbon materials, Carbon 39 (2001) 279–285.
13. Yang S, Lozano K, Lomeli A, Foltz HD, Jones R, Electromagnetic interference shielding effectiveness of carbon nanofiber/LCP composites, Compos. Part A-Appl. S. 36 (2005) 691–697.
14. Zhu S, Su CH, Lehoczky SL, Muntele I, Ila D, Carbon nanotube growth on carbon fibers, Diamond Relat. Mater. 12 (2003) 1825–1828.
15. Zhao ZG, Ci LJ, Cheng HM, Bai JB, The growth of multi-walled carbon nanotubes with different morphologies on carbon fibers, Carbon 43 (2005) 651–673.
16. Liu L, Zhou K, He P, Chen T, Synthesis and microwave absorption properties of carbon coil-carbon fiber hybrid materials, Mater. Lett. 110 (2013) 76–79.
17. Liu L, He P, Zhou K, Chen T, Microwave absorption properties of carbon fibers with carbon coils of different morphologies (double microcoils and single nanocoils) grown on them, J. Mater. Sci 49 (2014) 4379–4386.
18. Smits F, Measurement of sheet resistivities with the four-point probe, Bell Labs Tech. J. 37 (1958) 711–717.
19. M. Kawaguchi, K. Nozaki, S. Motojima, and H. Iwanaga, A growth mechanism of regularly coiled carbon fibers through acetylene pyrolysis, J. Cryst. Growth, 118 (1992) 309–313.
20. Kang G.-H, Kim S.-H, Effect of incorporating carbon nanocoils on the efficiency of electromagnetic-wave shielding of carbon-nanomaterial composites, Appl. Surf. Sci. 380 (2016) 114–118.
21. Simon R.M, Emi shielding through conductive plastics, Polym. Plast. Technol. Eng. 17 (1981) 1–10.

DOI: https://doi.org/10.26799/cp-sfkorea2017

Tables

Table 1. Experimental conditions for samples I – VII.

Sample	C_2H_2 flow rate (sccm)	CS_2 flow rate (sccm)	Total pressure (torr)	Total injection time (min)		Number of CS_2 on/off cycles	Substrate temp (℃)
				C_2H_2	CS_2		
I	500	20	100	100	100	0	750
II	500	60	100	100	100	0	750
III	500	100	100	100	100	0	750
IV	500	20	100	25	25	0	750
V	500	100 → 20	100	25	12.5	1	750
VI	500	100 → 20	100	50	25	2	750
VII	500	100 → 20	100	100	50	4	750

Table 2. Experimental conditions for samples A – D.

Sample	Composition by weight (%)			Type of composition
	CMC	CNC-CMC hybrid	PU	
A	-	~12	~88	CMC-CNC@PU
B	-	~6	~94	CMC-CNC@PU
C	~12	-	~88	CMC@PU
D	~6	-	~94	CMC@PU

Figure captions

Fig. 1 Modulation of C_2H_2 and/or CS_2 gas flow (processes I–VII) for the preparation of samples I–VII.

Fig. 2 (a) The instrumental setup for measuring shielding effectiveness and (b) the coaxial transmission test specimen adhering to ASTM D4935-99.

Fig. 3 FESEM images of the surface morphologies of (a) sample I, (b) sample II, and (c) sample III. The insets (Fig. 3b-i, Fig. 3b-ii) in Fig. 3b and the inset in Fig. 3c show the magnified images of the dotted square areas in Figs. 3b and 3c, respectively. The inset (Fig. 3b-i) in Fig. 3 shows the gathering of the wave-like CNCs around the CMCs.

Fig. 4 FESEM images of the surface morphologies of (a) sample IV and (b) sample V. The inset in Fig. 4b shows the magnified image of the dotted square area in Fig. 4b.

DOI: https://doi.org/10.26799/cp-sfkorea2017

Fig. 5 FESEM images of the surface morphologies of (a) sample VI and (b) sample VII. The inset in Fig. 5a shows the magnified image of the dotted square area in Fig. 5a. The insets (Fig. 5b-i and Fig. 5b-ii) in Fig. 5b show the magnified image of the dotted square area in Figs. 5b and 5b-i, respectively.

Fig. 6 TEM image of the carbon filaments constituting the CNC-CMC hybrid materials (sample VI). The inset in Fig. 6 shows the magnified image of the dotted square area in Fig. 6. It shows the existence of the heads of the wave-like CNCs at the outside of the CMC and the attachment of the wave-like CNCs onto the surface of CMC.

Fig. 7 (a) FESEM image of CNCs in sample VI and (b) The histogram plots for C, O, and Ni elements at the circle area and at the square area.

Fig. 8 FESEM images of the CMCs having different developing states of CNCs in sample V. It shows the development of the CNCs directly from the surface of the a-carbon structure constituting the CMC.

Fig. 9 The variation of the resistivity for sample I (CMCs-only sample) and sample VII (CNC-CMC hybrid sample) with increasing the operating temperature from 20°C to 300°C under vacuum condition.

Fig. 10 Total thickness of the coating layers for samples A–D as a function of the number of coatings.

Fig. 11 The SE variations of samples A–D having the similar layer thickness (~3mm) with increasing operating frequency.

Fig. 12 The SE values of samples A and C with thickness of 0.8–3.1 mm in the operating frequency range of 1.25–4.0 GHz.

DOI: https://doi.org/10.26799/cp-sfkorea2017

Figures

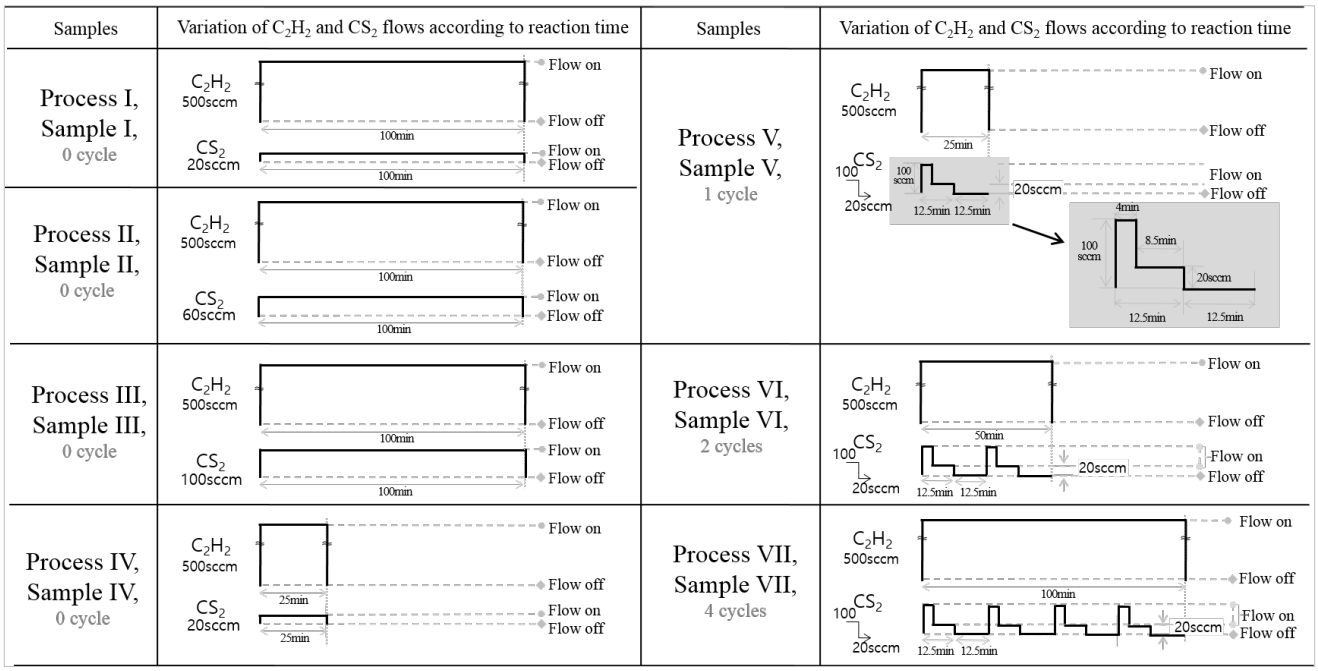

Fig. 1

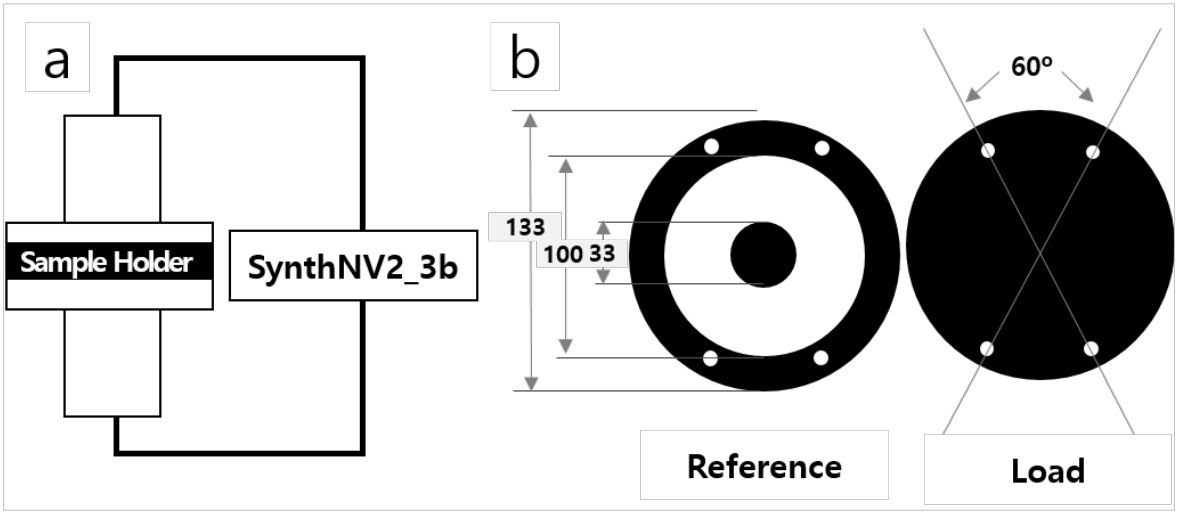

Fig. 2

DOI: https://doi.org/10.26799/cp-sfkorea2017

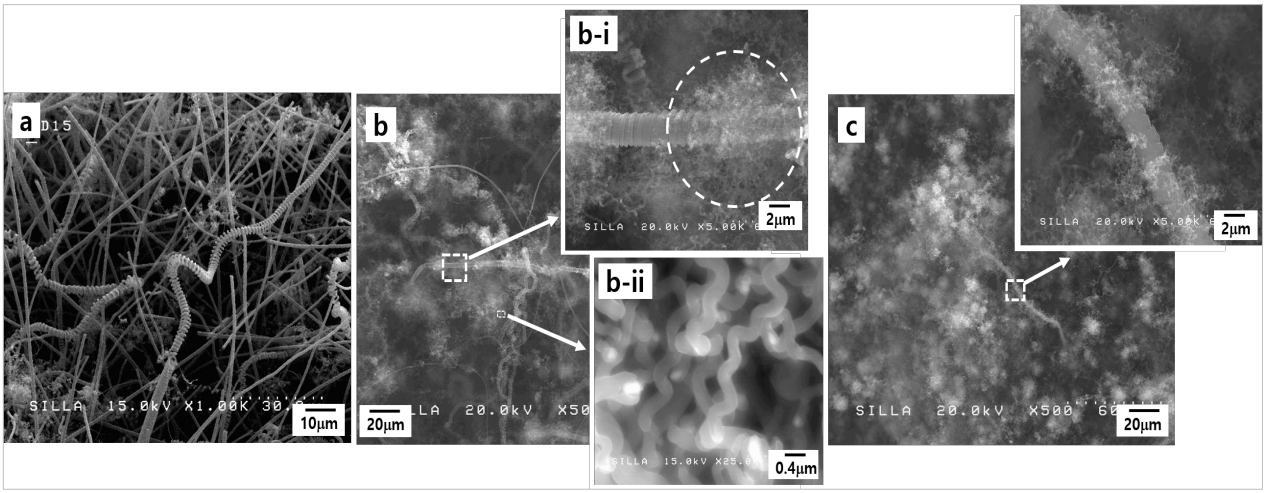

Fig. 3

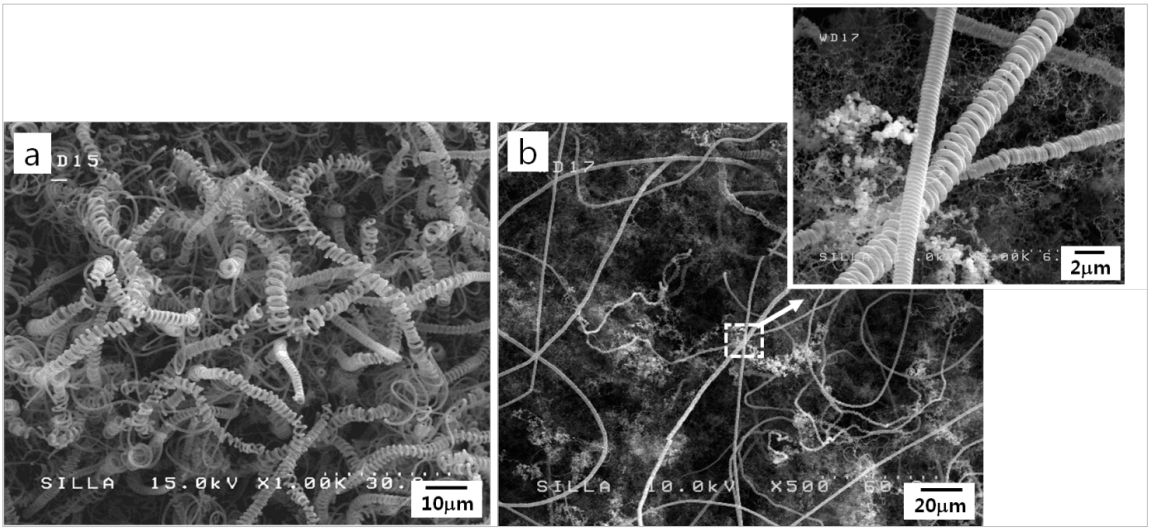

Fig. 4

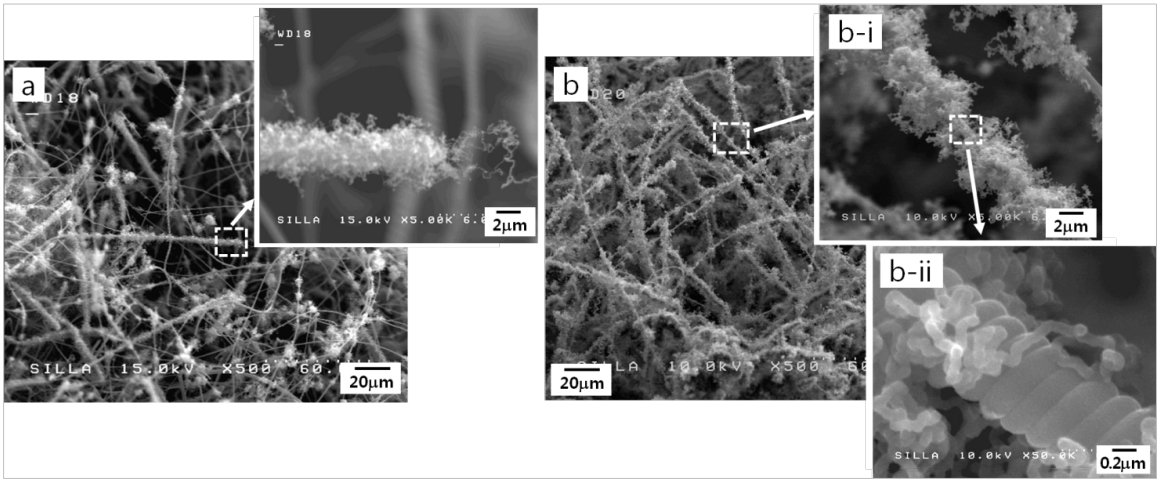

Fig. 5

DOI: https://doi.org/10.26799/cp-sfkorea2017

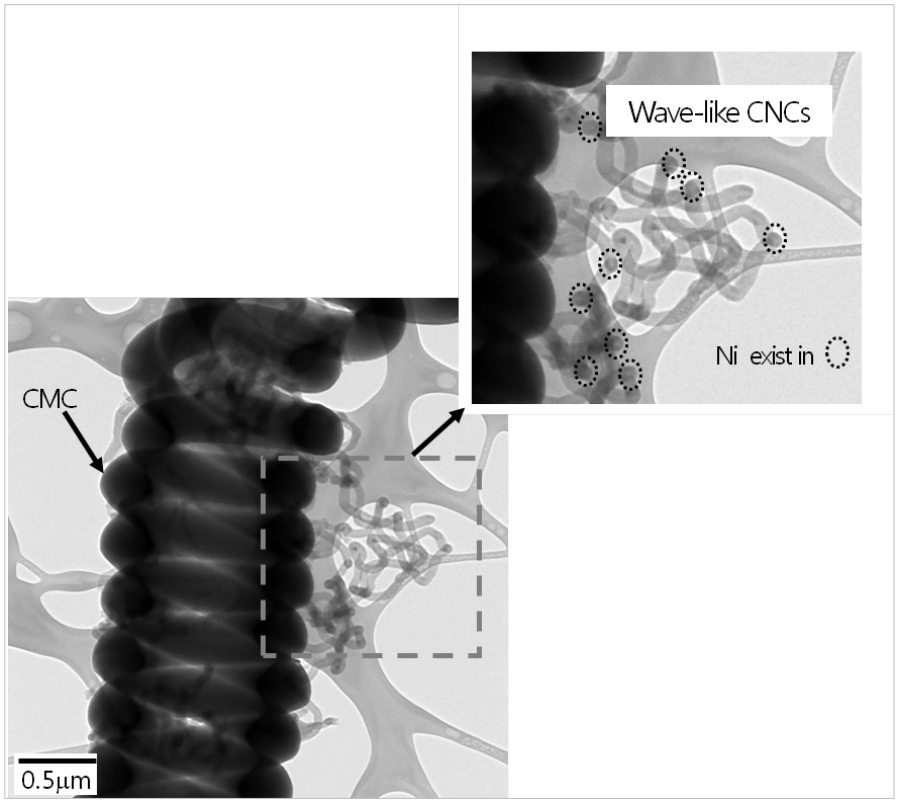

Fig. 6

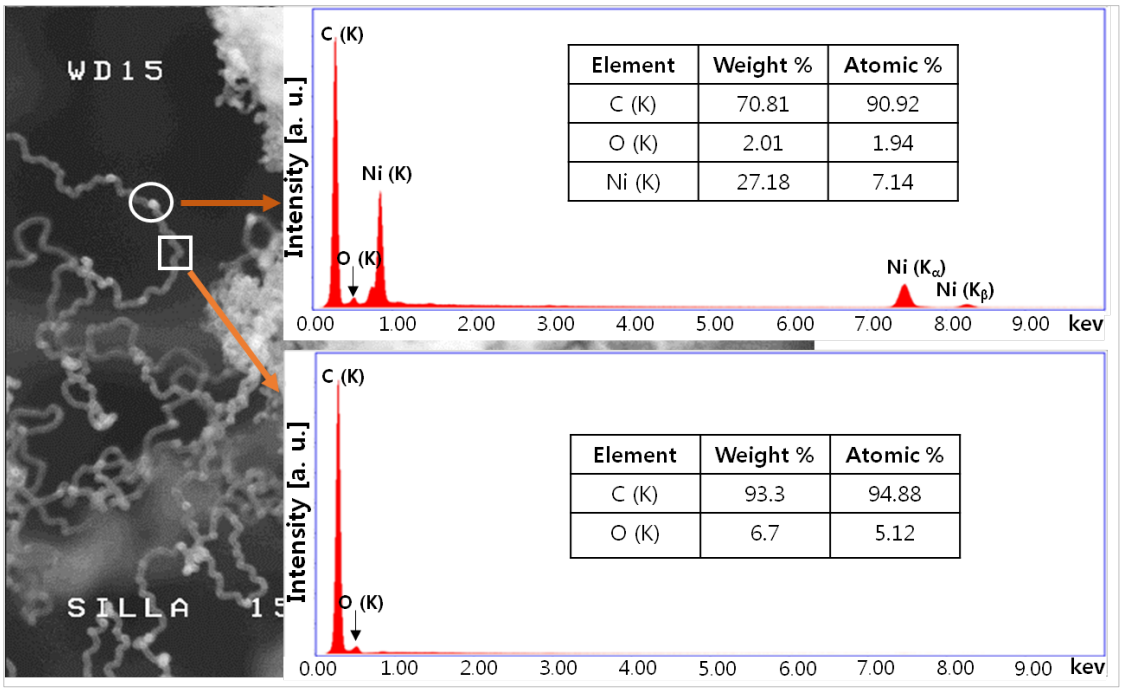

Fig. 7

DOI: https://doi.org/10.26799/cp-sfkorea2017

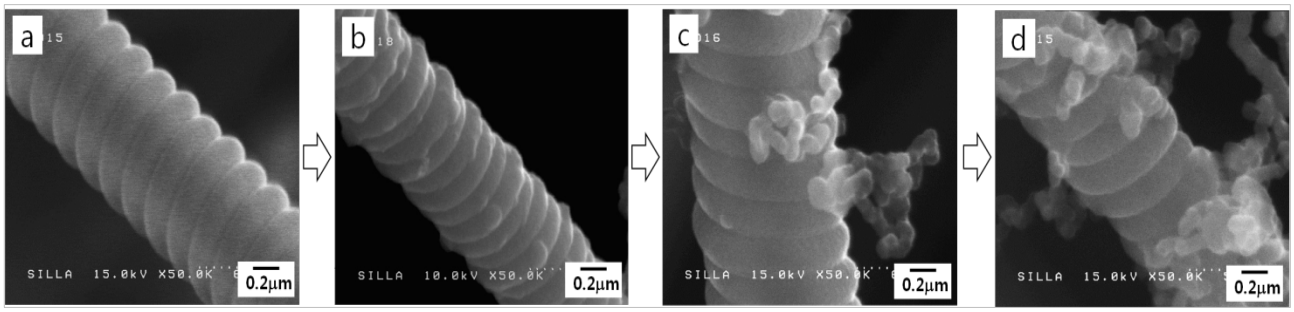

Fig. 8

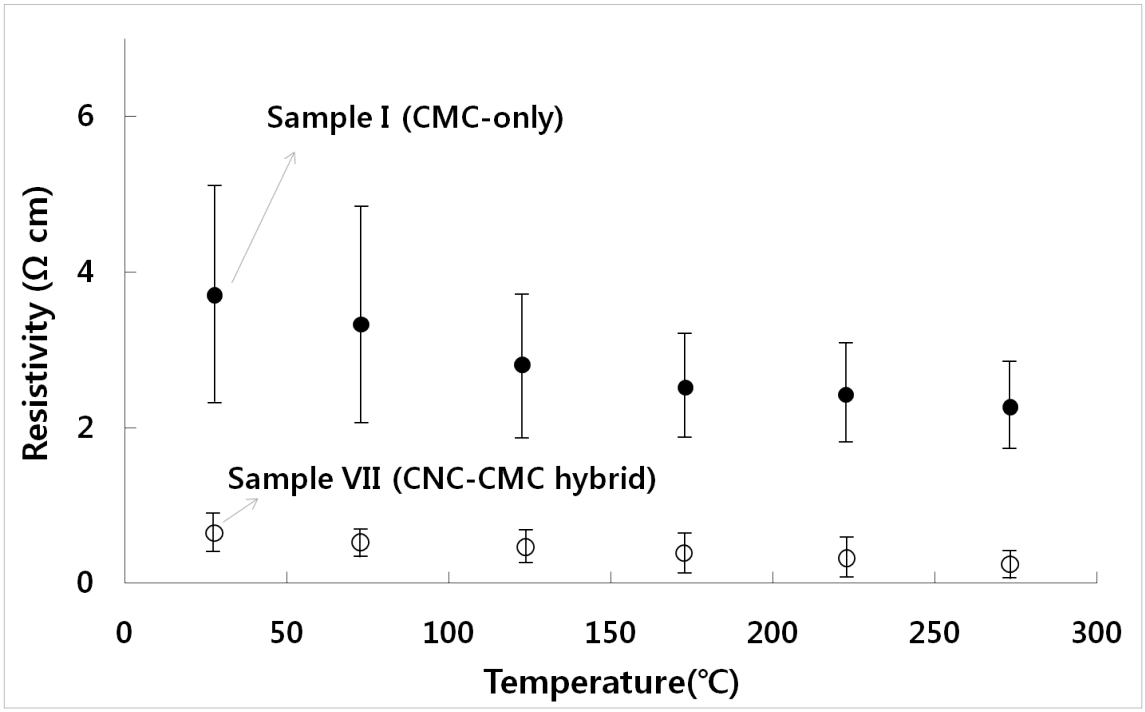

Fig. 9

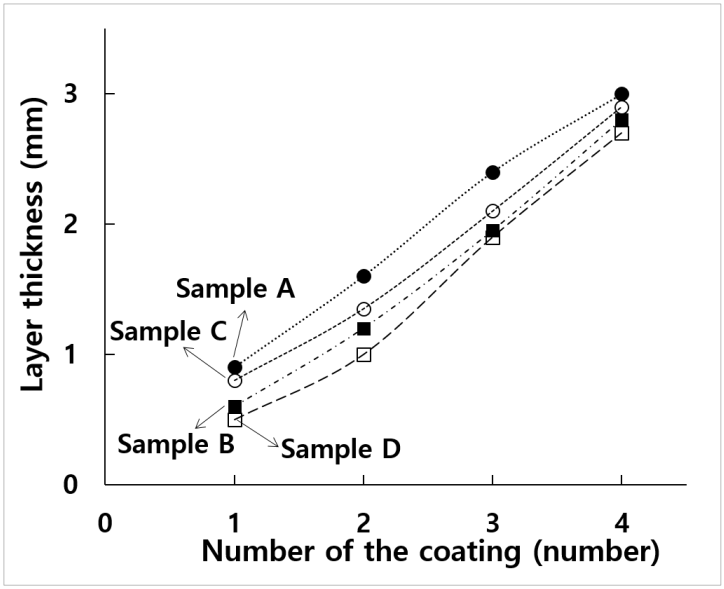

Fig. 10

DOI: https://doi.org/10.26799/cp-sfkorea2017

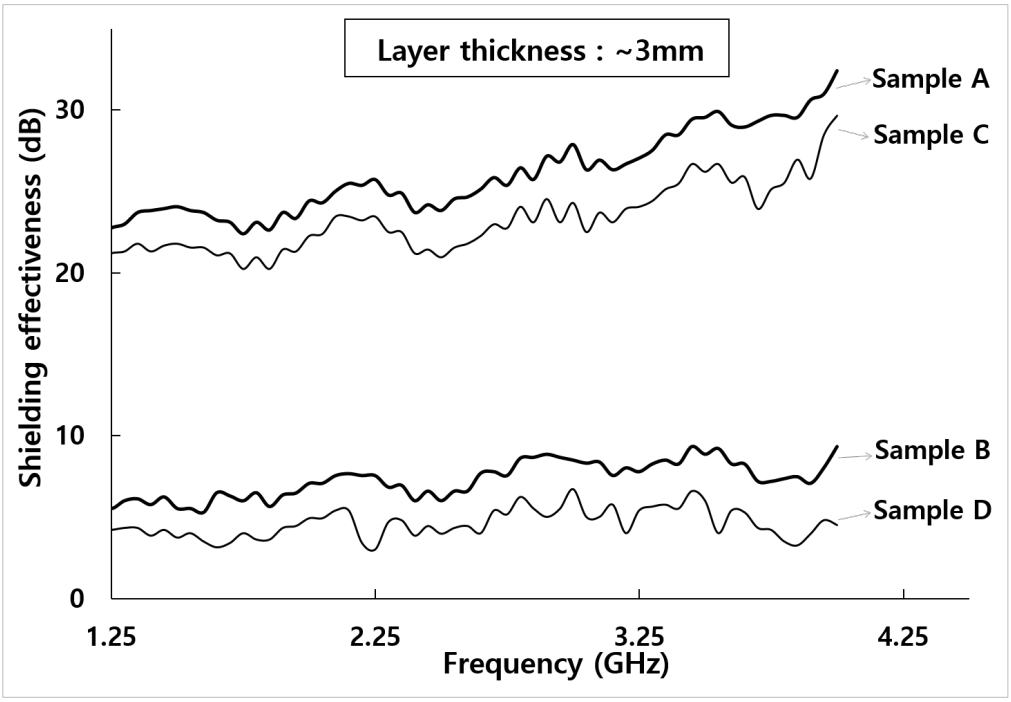

Fig. 11

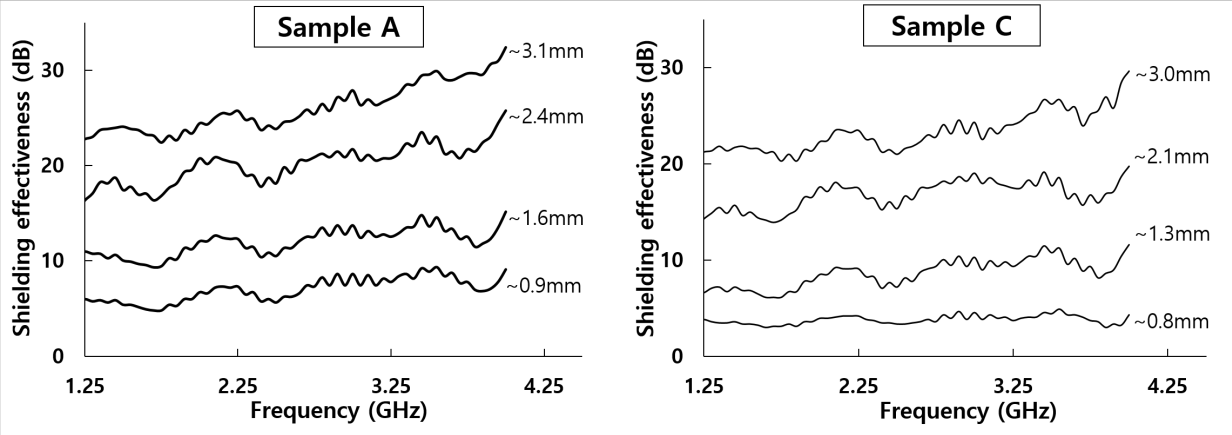

Fig. 12

Proceedings of the the International Conference on Surfaces, Coatings and Interfaces (SurfCoat Korea 2017)
Incheon - Rep. of Korea – Mar 29 – 31, 2017
DOI: https://doi.org/10.26799/cp-sfkorea2017

Performance of Anti-Biofouling Barriers on Nano-Engineered Metal Surfaces

K. Song,[1] J. Shim,[1] J-Y. Jung,[2] C. Lee[1] and Y. Nam[1,*]

[1] Kyung Hee University, Department of Mechanical Engineering, Yongin, Republic of Korea
[2] Korea Research Institute of Ships and Ocean Engineering, Technology Center for Offshore Plant Industries, Daejeon, Republic of Korea

Abstract:
In this work, we apply superhydrophilic, superhydrophobic and lubricant-impregnated wettability on aluminum (A1050), stainless steel (SUS-430) and Titanium (Ti) substrates, and investigate the anti-biofouling behaviors of such surface treatment. We fabricated nanostructures on three different metal surfaces using oxidation process, which can turn the surface into superhydrophilic (SHPi). Figure 1 shows the FE-SEM images of the investigated surfaces including oxide structure of A1050, SUS-430, and Ti. Then a silane (1H,-1H,2H,2H Perfluorodecyltrimethoxysilane) was vapor-deposition on the surface to induce superhydrophobicity (SHPo). In addition, silicone 100cst oil was infused on superhydrophobic surface to obtain the lubricant-impregnated slippery surface (LIS). Figure 2 shows the static and dynamic contact angles of the each investigated surfaces. The static contact angle of SHPi is <5° by the formation of thin water layer into nanostructures. Meanwhile, SHPo has stable air layer into nanostructures and it enables large contact angle (>150°) on the surface. In case of LIS, the thin lubricant layer covers nanostructures and it makes extremely small contact angle hysteresis (<5°) by its water repellency. Such three surfaces have different anti-biofouling barrier (SHPi, SHPo and LIS have the thin water layer, the air layer, and the lubricant layer, respectively). *Pseudomonas aeruginosa (P.aeruginosa)* attachment under static condition. For fluorescence imaging of attached bacterial cells, the substrates were stained with SYTOX green nucleic acid stain as shown Figure 3. Using the Image J analysis, covered area was extracted from the samples with different wetting characterestics, and their anti-fouling performance was quantitatively compared with that of Bare sample (Figure 4-6). The measured covered area shows that the biofouling behaviors are different depending on the substrates. In addition, the results show that the thin water layer of SHPi can improve the anti-fouling performance during initial time (8-12hours). When the superhydrophobicity was induced by the silane treatment, the SHPo shows the enhancement of the anti-fouling performance by 12~24hours. The LIS maintains the covered area of <10% regardless of test substrates and shows the highest anti-biofouling performance all the time. Eventually, the oil layer on LIS, the air layer on SHPo, and the thin water layer on SHPi show better anti-biofouling performance in order.
Our work provides the strategies to increase the anti-biofouling and it will help to develop improved surface modification techniques under various environment.

Keywords: Surface modification, Nanostructure, Chemical vapor deposotion, Lubricant impregnated surface, Wettabilities, Anti-Fouling, Bacteria adhesion, Pseudomonas aeruginosa.

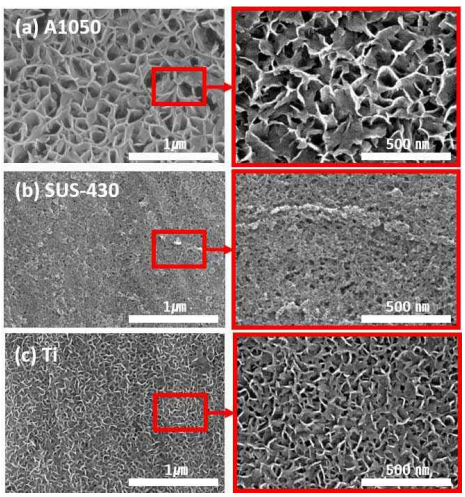

Figure 1: FE-SEM images of the oxidation scheme applying A1050(a), SUS-430(b), and Ti(c) samples.

DOI: https://doi.org/10.26799/cp-sfkorea2017

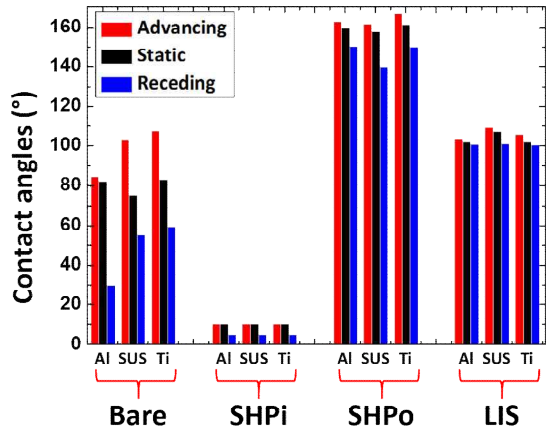

Figure 2: Contact angles of the investigated samples with wetting characterestics.

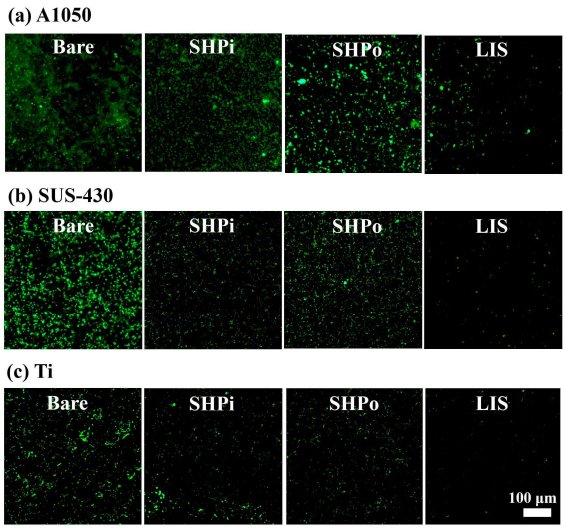

Figure 3: Fluorescence images of *P.aeruginosa* attachment on A1050(a), SUS-430(b), and Ti(c) surfaces after 12hour in fouling medium, respectively.

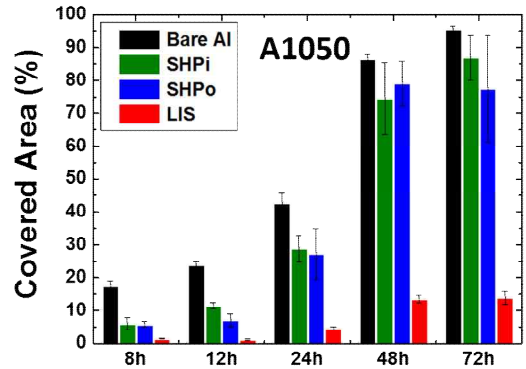

Figure 4: Proliferation of *P.aeruginosa* attachment on A1050 surfaces in fouling medium.

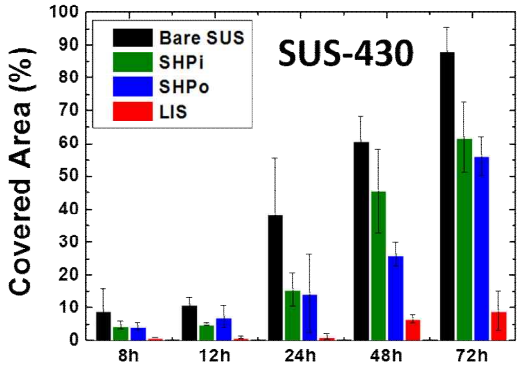

Figure 5: Proliferation of *P.aeruginosa* attachment on SUS-430 surfaces in fouling medium.

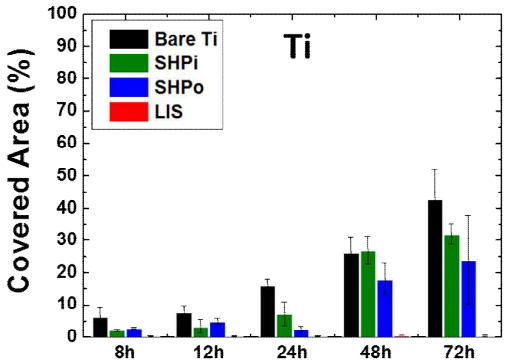

Figure 6: Proliferation of *P.aeruginosa* attachment on Ti surfaces in fouling medium.

Acknowledge:

This work was supported by Basic Science Research Program(2015R1A1A1A05001412) funded by the Ministry of Science, ICT and Future planning and the Korea Research Institute of Ships & Ocean Engineering(KRISO) Endowment Grant(No.pes2180).

References:

1. P. Tang, W. Zhang, Y. Wang, B. Zhang, H. Wang, C. Lin, L. Zhang. (2011) Effect of superhydrophobic surface of titanium on Staphylococcus aureus adhesion, *Nanomaterials.*, 2.
2. K. Epstein, T. Wong, A. Belisle, M. Boggs, J. Aizenberg. (2013) Liquid-infused structured surfaces with exceptional anti-biofouling performance, *PNAS.*, 109, 33, 13182-13187.

*Proceedings of the the International Conference on Surfaces, Coatings and Interfaces (**SurfCoat Korea 2017**)*
Incheon - Rep. of Korea – Mar 29 – 31, 2017
DOI: https://doi.org/10.26799/cp-sfkorea2017

Intrinsic Stresses in CrN and TiN Coatings Deposited by Vacuum Arc Method

A.I. Kalinichenko[1], S.S. Perepelkin[1], V.E. Strel'nitskij[1]
[1]National Science Center "Kharkov Institute of Physics and Technology", Kharkov, Ukraine

In the model of the nonlocal thermoelastic peak of low energy ion, formula for intrinsic stress in coating deposited from ion beam in the modes of the direct current and the pulsed bias potential is obtained. The stresses in the CrN (TiN) coating deposited by vacuum arc method from beam of Cr^+ (Ti^+) ions are calculated. It is shown that intrinsic stress significantly depends on material of the deposited coating and on the deposition mode. The calculated results in case of TiN coatings agree qualitatively with the experimental data.

1. Introduction

The coatings based on TiN and CrN, combining improved performance (hardness, wear resistanse, corrosion and radiation stability) formed by methods of vacuum-arc deposition [1]. Intrinsic stresses arising in films during vacuum-arc deposition can cause degradation of coatings [2]. Determination of intrinsic stress value and their dependence on thermal parameters of deposition process of coatings is needed to select the optimum mode of deposition.

According to model proposed in [2] the intrinsic stress is formed as result of stress generation due to defect formation during ion implantation and stress relaxation during migration defects in point thermal peaks (PTP) of ions. Formula obtained in [2] gave qualitative explanation of the observed stress dependence on the ion energy and satisfactory quantitative agreement with experimental results.

However, the use of PTP model for description of stress relaxation seems to be not quite correct, because it does not take into account the nature of interaction between the implanted ions and atoms of the target material, which determines the energy content and the size of the formed thermal peak. In this regard, the model can not explain the experimentally observed dependence of intrinsic stress on the deposition temperature T_0. Its agreement with experimental data is achieved by activation energy u at values of u = 3 … 14 eV, far exceeding the known values for defect migration. Besides the charge state of the ions and the deposition mode of coating do not take into account in the model.

In [3], the modified formula for intrinsic stress calculation which uses the model of nonlocal thermoelastic peak (NTP) of ion [4] is proposed. According to this model, the NTP of the low-energy ion is overheated and overpressured nanometer-sized region, arising around the ion path in the coating material as a result of thermalization of ion phonon losses. This formula allows us to calculate the stress in one-component coatings deposited from ion flows with different charging in modes of direct current (DC) and pulsed bias potentials and at different deposition temperatures.

We present the results of theoretical study of intrinsic stress σ in CrN (TiN) coatings, deposited by vacuum arc method from beam of Cr^+ (Ti^+) ions in pulsed potential mode and direct current (DC) mode and comparison the calculation results with experimental data.

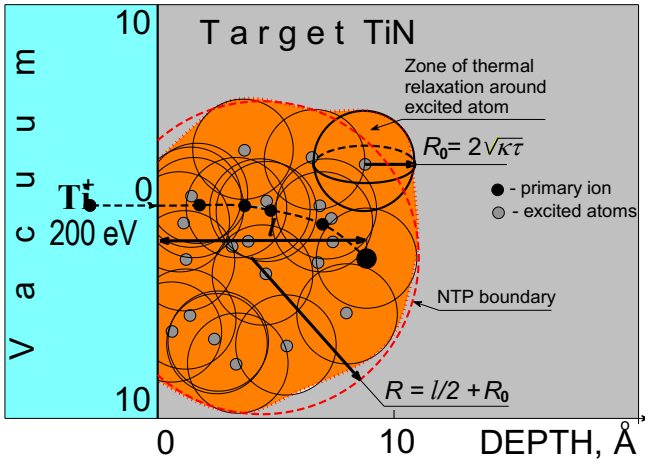

Fig. 1. Scheme of the ion NTP in the target material

2.Theory and Calculation

The theoretical model for calculation of σ is proposed in [3]. It is based on conception of non-local thermoelastic peak (NTP) of the ion which is approximated by spherical segment adjacent to the target surface. The main parameters of the NTP are the radius

$$R(E,t) = l(E)/2 + R_0(t) \qquad (1)$$

and the energy content

$$E_{ph} = \eta(E)E. \qquad (2)$$

Here $l(E)$ is the average projective range,

DOI: https://doi.org/10.26799/cp-sfkorea2017

and $\eta(E)$ is the relative part of phonon losses of the ion, calculated using the software package SRIM2000; $R_0(t) = 2\sqrt{\kappa(t+\tau)}$ is the radius of "smearing" of the point-like heat source for time t, κ is the thermal diffusivity, τ is the time of the ion-ion relaxation. The center of the NTP is situated in the middle of the average projected range of the ion l [4]. Fig. 2 displays functions $\eta(E)$, $l(E)$, $R_0(t)$ and $R(E,0)$ (curves 1 – 4, respectively) for NTP of the Ti^+ ion in TiN. Temperature of the target T_0 is equal to 473 K. Using $l(E)$ and E_{ph} we can determine NTP volume

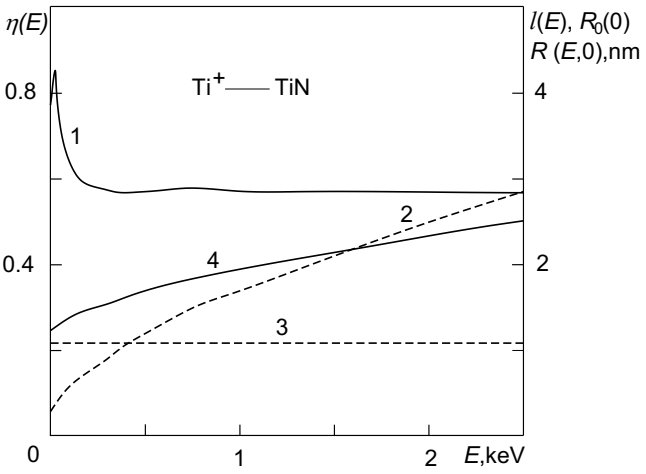

Fig. 2. Parameters of the NTP of Ti^+ ion in TiN depending on ion energy E.

$$V = 4\pi\left(R^3 - 3R_0^2 l/8 - R_0^3/2\right)/3 \quad (3)$$

and average temperature in NTP:

$$T(E,0,T_0) = E_{ph}(E)/\rho C V(E,t) + T_0, \quad (4)$$

where ρ, C and T_0 are the mass density, the specific heat and the initial temperature of target material, respectively.

Fig. 3 displays initial temperatures in NTPs of Ti^+ in TiN and Cr^+ in CrN.

Deriving of formula for intrinsic stress we followed the reasoning of C.A. Davis [2]. Intrinsic stress arises as a result of two opposite processes: 1) subsurface ion implantation and defect production, leading to volumetric strain origination, and 2) decrease of defect number due to their migration in ion NTPs and drain to boundaries. The last leads to stress relaxation.

The expression for compressive stress in coating deposited from the ion beam in the pulsed potential mode has form [3]:

$$\sigma(U) = A\frac{E_Y}{1-\Pi}\frac{ft_p\sum_i \chi_i\zeta\left(i\left(U+U_0+E_{0i}\right)\right)+\left(1-ft_p\right)\sum_i \chi_i\zeta\left(i\left(U_0+E_{0i}\right)\right)}{1+ft_p\sum_i \chi_i w\left(i\left(U+U_0+E_{0i}\right)\right)+\left(1-ft_p\right)\sum_i \chi_i w\left(i\left(U_0+E_{0i}\right)\right)}, \quad (5)$$

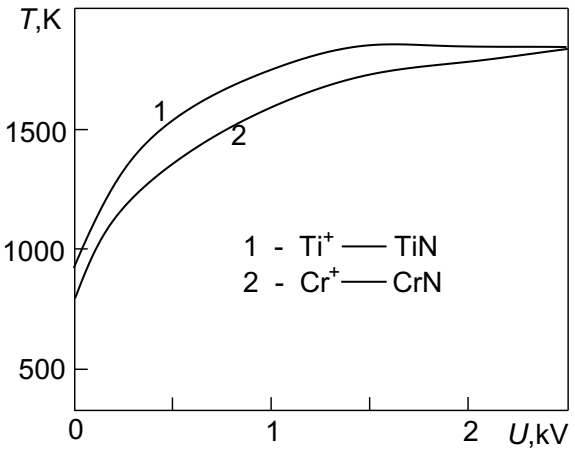

Fig. 3. Initial temperatures in NTPs of Ti^+ in TiN (curve 1) and Cr^+ in CrN (curve 2).

where E_Y and Π are the Young modulus and the Poisson ratio of target material, t_p is the duration of pulse with amplitude U, f is the repetition frequency of pulses, U_0 is the floating potential, i is the ion charge (in units of the proton charge), E_{0i} is the reduced (per unit charge) initial energy of the ion having charge i and T_0 is the temperature of unirradiated target. The parameter A is the adjustable parameter which is defined from experimental data [5]; $\zeta(E)$ is the number of point defects produced by ion with energy E, $w(E,u,T_0)$ is the number of thermoactivated transitions at activation energy of defect migration u in the ion NTP with energy E:

$$w(E,u,T_0) = n_0\nu\int_0^{\tau_c} V(t,E)\, e^{-\frac{u}{k_B T(t,E,T_0)}}\, dt. \quad (6)$$

DOI: https://doi.org/10.26799/cp-sfkorea2017

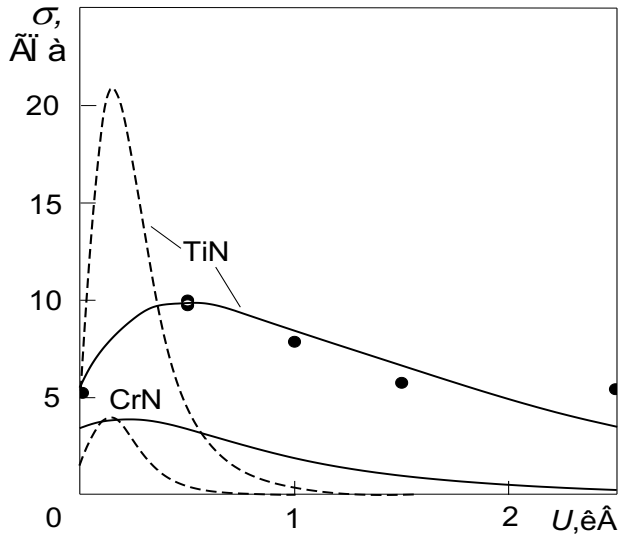

Fig. 4.: Intrinsic stresses in TiN and CrN coatings. Continuous (dashed) curves correspond to the pulsed potential mode (to DC mode). Black symbols are the experimental data [5].

Here k_B is the Boltzmann constant, n_0 is the concentration of atoms in the target, ν is the frequency of atomic oscillations, τ_c is the life time of NTP (i.e., the time of the NTP cooling).

Table 1
Parameters for stress calculation

Coating	τ	U_1, V	u, eV	T_0, K
TiN	1	0	0,75	473
TiN	0,12	0	0,75	473
CrN	1	0	0,75	473
CrN	0,144	100	0,75	473

Note that the case $ft_p = 1$ corresponds to direct current (DC) mode of deposition.

Fig. 4 displays functions $\sigma(U)$ in TiN (CrN) coatings at deposition of ions Ti (Cr) in pulsed potential mode (solid curves) and DC mode (dashed curves). Parameters for stress calculation are given in table 1.

It is shown that intrinsic stress significantly depends on material of the deposited coating and on the operating mode of deposition.

3. Conclusions

1. Within the NTP model of low-energy ion the expression for intrinsic stress in coating deposited from ion beam is obtained. The expression accounts for the presence of ions with different charges.It is valid in the modes of both DC and pulsed potential.
2. Comparison of calculation results of intrinsic stress in TiN coatings deposited from the Ti ion beam with experimental data shows their qualitative agreement. Deposition in the pulsed potential mode leads to significantly less maximum stress than deposition in the DC mode at the same temperature. Comparison of intrinsic stresses in TiN and CrN coatings shows that maximum stress $\sigma_{\max} = \sigma(U_m)$ and potential U_m significantly depend on material of the deposited coating and on the operating mode of deposition.
3. The pulsed potential mode allows to produce coatings with low intrinsic stress at relatively low deposition temperatures which eliminates the chemical decomposition and/or phase separation in the deposited coating. Also, this operational mode allows using substrates with relatively low tempering temperatures.

References

1. Veprek S., Veprek-Heijman M., Karvankova P., Prochazka J., Thin Solid Films. 476 (2005) 1-29.
2. Davis C.A., Thin Solid Films. 226 (1993) 30 - 34.
3. Kalinichenko A.I., Kozionov S.A., Perepelkin S.S., Strel'nitskij V.E., Proceedings of the international conference Nanomaterials: Applications and Properties. 3/1(2014)01PCSI15(4pp).
4. Kalinichenko A.I., Perepelkin S.S., Strel'nitskij V.E., Diamond Relat. Mater. 15 (2006) 365-370.
5. Akkaya S.S., Vasyliev V.V., Reshetnyak E.N et. al., Surf. Coat. Technol. 236(2013)332.